Trabajo de Fin de Grado

Grado en Física

WAVE PROPAGATION IN SIMULATIONS OF SUNSPOTS

supervised by: Tobías Felipe García

cosupervised by: Elena Khomenko Shchukina

submitted on: 09/06/2021

submitted by: Guillem Castelló i Barceló
alu0101162256@ull.edu.es

Abstract

Este trabajo de fin de grado está principalmente centrado en el estudio de ondas en manchas solares a partir de los resultados obtenidos en simulaciones numéricas.

En primer lugar se obtuvieron los parámetros típicos para la caracterización de las ondas que se propagan en las manchas solares, como la velocidad del sonido, velocidad Alfvén y plasma-beta, entre otros.

Se utilizó el análisis de Fourier para calcular los espectros de potencia a diferentes alturas y los espectros de diferencia de fase y amplificación entre las oscilaciones de velocidad medidas en dos capas. Estas medidas sirven para caracterizar cómo se propagan las ondas dentro de la simulación de la mancha solar.

Estos resultados se compararon con los esperados por el marco teórico de propagación de ondas. Se estudiaron de forma analítica tres casos específicos correspondientes a atmósferas adiabáticas con y sin estratificación gravitatoria y a atmósferas estratificadas con pérdidas radiativas. En el último caso, la propagación de ondas entre dos capas se puede caracterizar por medio de tres parámetros: el tiempo de relajación, la diferencia de altura y la altura de escala. Los datos de la simulación se compararon con los resultados teóricos.

En la fotosfera, las medidas de la simulación muestran un buen acuerdo con el modelo teórico de propagación de ondas. Por el contrario, los espectros medidos en la cromosfera presentan un comportamiento que no se puede explicar con un modelo de propagación de ondas. En los espectros de amplificación hay zonas donde la amplitud es mínima, cuya frecuencia coincide con la existencia de saltos en el espectro de diferencia de fase. Ambas medidas son consistentes con la existencia de ondas estacionarias.

En conclusión, el estudio de las oscilaciones en una simulación numérica de la umbra de una mancha solar muestra que las ondas se propagan desde la fotosfera hasta la baja cromosfera. En capas altas cromosféricas, las oscilaciones presentan indicios de tratarse de ondas estacionarias y apuntan a la presencia de una cavidad resonante producida por la reflexión de las ondas en los gradientes de temperatura de la región de transición.

Todos los cálculos de este estudio se han realizado usando $Python$, en concreto con el módulo $Numpy$ [1]. No se ha necesitado mucho poder de cómputo en general debido al carácter de la simulación.

Contents

List of Figures

List of Tables

1 Introduction

The Sun is the main astronomical object of the Solar System and, as such, it has caught the attention of humanity, and made them try to understand it. Astronomers found that the Sun had vanishing darker spots over the brighter background surface. These spots are now known as sunspots.

Sunspots are a temporary phenomena observed in the Sun. At the photosphere, they appear darker than the background since the temperature of the surface is reduced, mostly due to concentrations of magnetic field flux, usually shaped as tubes [2].
Sunspots are characterized by two main regions, the umbra and the penumbra. The structure of these regions is quite different, due to the different magnetic configurations they have. The umbra has a mainly vertical magnetic field, and the penumbra has highly inclined magnetic field.

In recent years, observations and theoretical modeling of sunspots have greatly progressed. It is possible to study sunspot waves from the photosphere to upper coronal layers. Waves in different layers have different behaviours. They exhibit differences in the amplitude and period of the oscillations.
In observations, the different properties of waves can be determined using spectroscopic and imaging instruments. These studies benefit from the simultaneous analysis of different spectral lines formed at different atmospheric heights. [3]

1.1 Waves in sunspots

Wave propagation phenomena at different regions of the sunspots are related with each other, as many observational studies have pointed out. Their study requires the identification of the different wave modes present in magnetized-media (fast and slow magnetoacoustic modes and Alfvén modes) since they exhibit different wave properties.
The nature of sunspot waves depends on the plasma parameter β (ratio between the gas pressure and the magnetic pressure), which separates regions with distinct physics i.e. $\beta < 1$, $\beta = 1$ and $\beta > 1$.

In this study, we will analyze regions with plasma parameter β less than unity, the upper photosphere, chromosphere and corona, from a sunspot umbra. We will focus on the first two regions.

Oscillations in these layers have well-known characteristics:

- Photospheric umbral oscillations: 5-minute period and small amplitude when compared to the quiet Sun around the sunspots [4]. Spectral measurements of them have been done mainly for sunspots situated near the solar disc center, so the velocity direction was nearly parallel to the sunspot magnetic field.
- Chromospheric umbral oscillations: 3-minute oscillations with larger amplitudes when compared to photospheric oscillations. Umbral flashes (sudden increases in brightness in the core of the Ca II K_{2V} line) are the main manifestation of the oscillations at chromospheric layers. [5] [6]

The consensus is that the observed oscillations are mainly slow-magnetoacoustic waves travelling along the magnetic field line at the sound speed [2]. This consensus was obtained via the analysis of numerous observations, theoretical modeling, and numerical simulations.

As waves propagate from the photosphere to the chromosphere, the media they find has a reduction in density. The amplitude of the oscillations increases to maintain the kinetic energy flux. When their amplitude is comparable to the propagation velocity of the waves (sound speed for slow magnetoacoustic waves in low-β plasma), they develop into shocks. These shocks are speculated to be one of the main heating mechanisms [7] [8] of the chromosphere.

1.2 Chromospheric acoustic resonator.

One of the proposed models for the solar atmosphere is the chromospheric resonant cavity model [9] [10]. In this model, temperature gradients at the photosphere and transition region form the boundaries of a resonant cavity.
In this model, vertical propagating waves can reflect at these temperature gradients, and form standing waves at the chromosphere.

This model has been a matter of debate over the years (see Section 7.4 from [2] for a discussions of the historical evolution). Some authors have presented contradictions between the predicted results and the observational data [11] [12] [13]. Recently, new works have shown evidences supporting the chromospheric resonant cavity model. They are founded on the presence of high frequency power peaks [14] and the analysis of oscillatory phases [15].

1.3 Objectives of this work

The main objective of this work is the analysis of wave propagation in a simulation of a sunspot, identifying the behaviour of waves at different atmospherics layers. Also, we want to evaluate the chromospheric resonances. With this aim, we have compared the measurements from the numerical simulation, where a chromospheric resonant cavity is present and standing oscillations are expected, with those predicted by analytical models of wave propagation.
This work will try to explain this difficult field of astrophysics to readers not familiarized with it, explaining the theoretical basis of wave propagation, applied to the solar atmosphere.

We will begin by presenting the theoretical models of wave propagation we considered for this work. Then, we will explain the simulation used for the study and, finally, the spectral analysis of the waves in the simulation is discussed.

2 Theoretical background

In this chapter, we will present the theoretical expressions needed to describe the different types of waves we will study.

The basic system of equations is:

$$\begin{cases} \frac{\partial \rho}{\partial t} + \vec{\boldsymbol{\nabla}}(\rho \vec{v}) = 0 \\ \frac{\partial}{\partial t}(\rho \vec{v}) = -\vec{\boldsymbol{\nabla}}(\rho \vec{v} \otimes \vec{v} + P\vec{I}) + \rho \vec{g} \\ \frac{\partial}{\partial t}\left(\rho\epsilon + \rho\frac{v^2}{2}\right) = -\vec{\boldsymbol{\nabla}}\left[(\rho\frac{v^2}{2} + \rho\epsilon + P)\vec{v}\right] + Q_{rad} + \vec{g}\cdot\vec{v} \end{cases} \tag{2.1}$$

These are the continuity equation, the momentum equation, and the energy equation, respectively, and ρ represents the density, P the pressure, $\vec{v}$ the velocity, ϵ the internal energy, I is the unit 3×3 matrix, $\vec{g}$ is the gravity vector, and finally Q_{rad} is the term representing radiative interactions.

2.1 Non-stratified acoustic waves.

In this approximation we are not considering gravity nor magnetic fields. Also, we are considering ideal gases and the adiabatic approximation ($Q_{rad} = 0$).

Applying small-perturbation analysis, we consider an equilibrium situation (static) where a small perturbation is applied that changes the values of $\vec{v}$, P, ρ in time and position. Doing so and linearizing (rejecting second and greater order terms on the perturbation) we obtain the following:

$$\begin{cases} \frac{\partial \rho'}{\partial t} + -\rho_0 \vec{\boldsymbol{\nabla}}(\vec{v}') = 0 \\ \rho_0 \frac{\partial}{\partial t}(\vec{v}') = -\vec{\boldsymbol{\nabla}}(P') \\ \frac{\partial}{\partial t}(\rho\epsilon)' = -(\rho_0\epsilon_0 + P_0)\vec{\boldsymbol{\nabla}}\vec{v}' \end{cases} \tag{2.2}$$

Where the primed variables represent the perturbed values of them and the sub 0 index represent the initial conditions.

Defining the sound speed c_{s0} as $c_{s0} = \left(\gamma \frac{P_0}{\rho_0}\right)^{1/2}$, one can rewrite the equations as follows:

$$\begin{cases} \frac{\partial}{\partial t}\left(\frac{\rho}{\rho_0}\right) = -c_{s0}\vec{\boldsymbol{\nabla}}(\frac{\vec{v}'}{c_{s0}}) \\ \frac{\partial}{\partial t}\left(\frac{\vec{v}'}{c_{s0}}\right) = -\frac{c_{s0}}{\gamma}\vec{\boldsymbol{\nabla}}(\frac{P'}{P_0}) \\ \frac{\partial}{\partial t}\left(\frac{P'}{P_0}\right) = -\gamma c_{s0}\vec{\boldsymbol{\nabla}}(\frac{\vec{v}'}{c_{s0}}) \end{cases} \tag{2.3}$$

Operating one obtains the following wave equations:

$$\begin{cases} \frac{\partial^2}{\partial t^2}p' = {c_{s0}}^2\ \nabla^2 p' \\ \frac{\partial^2}{\partial t^2}\rho' = {c_{s0}}^2\ \nabla^2 \rho' \\ \frac{\partial^2}{\partial t^2}\vec{v}' = {c_{s0}}^2\ \nabla^2 \vec{v}' \end{cases} \tag{2.4}$$

The natural procedure from here is to try Fourier modes in space and time, i.e. solutions of the form:

$$\vec{v}' = \vec{A}e^{i(\vec{k}\cdot\vec{r}-\omega t)} \tag{2.5}$$

$$P' = Be^{i(\vec{k}\cdot\vec{r}-\omega t)} \tag{2.6}$$

$$\rho' = Ce^{i(\vec{k}\cdot\vec{r}-\omega t)} \tag{2.7}$$

The acoustic waves are isotropic, in the sense that there is no privileged direction, as for example would be the direction of gravity or the magnetic field. Therefore, one can freely choose the axis z as the direction of the wave propagation. In the case there is magnetic field, one of the modes (slow magneto-acoustic mode in low plasma beta) has similar properties to an acoustic mode, but it is forced to propagate along the magnetic field direction.

We can obtain the dispersion relations, which characterizes the waves:

$$k^2 = \frac{\omega^2}{{c_{s0}}^2} \tag{2.8}$$

From (2.8) we see that in this case the waves propagate with speed c_{s0}, since this value does not depend on k all modes travel at the same speed.

We obtain solutions:

$$v_z = Ae^{ikz}e^{-i\omega t} = A(z)e^{\pm i\frac{\omega}{c_{s0}}z}e^{-i\omega t} \tag{2.9}$$

Where the positive solution of the dispersion relation is for upward propagating waves.

2.2 Adiabatic acoustic-gravity waves

Now we will consider an atmosphere where gravity takes and important role, stratifying it. We will maintain the adiabatic approximation ($Q_{rad} = 0$).

From the system of equations (2.1), manipulating it we can arrive to the following differential equation for the velocity:

$$\frac{\partial^2 \vec{v}}{\partial t^2} = c_{s0}^2 \vec{\boldsymbol{\nabla}}(\vec{\boldsymbol{\nabla}} \cdot \vec{v}) + (\gamma - 1)\vec{g}(\vec{\boldsymbol{\nabla}} \cdot \vec{v}) + \vec{\boldsymbol{\nabla}}(\vec{v} \cdot \vec{g}) \tag{2.10}$$

This partial differential equation with constant coefficients for the velocity accepts harmonic solutions, like the ones presented in Eq. 2.5.

Using this trial function in equation 2.10 we obtain a vectorial dispersion relation:

$$-\omega^2 \vec{v} = -c_{s0}^2 \vec{k}(\vec{k} \cdot \vec{v}) + i(\gamma - 1)\vec{g}(\vec{k} \cdot \vec{v}) + i\vec{k}(\vec{g} \cdot \vec{v}) \tag{2.11}$$

From this relation we can see that there are only 2 independent directions, the Z-direction (the one where the gravity is not null) and one perpendicular to it, the X-direction. The scalar dispersion relations can be obtained projecting in those directions.

$$-\omega^2 v_x = -c_{s0}^2 k_x(\vec{k} \cdot \vec{v}) - ik_x(gv_z) \tag{2.12}$$

$$-\omega^2 v_z = -c_{s0}^2 k_z(\vec{k} \cdot \vec{v}) - i(\gamma - 1)g(\vec{k} \cdot \vec{v}) - ik_z(gv_z) \tag{2.13}$$

Developing the dot products and grouping terms one obtains:

$$(\omega^2 - c_{s0}^2 k_x^2)v_x = (c_{s0}^2 k_x k_z + ik_x g)v_z \tag{2.14}$$

$$(c_{s0}^2 k_x k_z + i(\gamma - 1)k_x g)v_x = (\omega^2 - c_{s0}^2 k_z^2 - ik_z g)v_z \tag{2.15}$$

We have two equations for two variables (components of velocity). Non-trivial solutions can be obtained if the determinant is zero.

$$\begin{vmatrix} -(\omega^2 - c_{s0}^2 k_x^2) & (c_{s0}^2 k_x k_z + ik_x g) \\ (c_{s0}^2 k_x k_z + i(\gamma - 1)k_x g) & -(\omega^2 - c_{s0}^2 k_z^2 - ik_z g) \end{vmatrix} = 0 \tag{2.16}$$

From this determinant arises a dispersion equation of 4th order, i.e. admits 4 solutions:

$$\omega^4 - \Big[c_{s0}^2(k_x^2 + k_z^2) + ig\gamma k_z\Big]\omega^2 + (\gamma - 1)g^2 k_x^2 = 0 \tag{2.17}$$

From this dispersion equation we can conclude:

- k_z is complex. The waves will be weakened or amplified in space or time.
- The propagation velocity will depend on the frequency and $\vec{k}$. The waves are dispersive, unlike the non-stratified case.
- The wave amplitude will increase with height, this will be shown later.

Choosing the frequency as a real number (there is no attenuation in time), and splitting k_z into real (k_{zr}) and imaginary (k_{zi}) parts, the dispersion relation transforms into:

$$\omega^4 - \left[c_{s0}^2(k_x^2 + k_{zr}^2 - k_{zi}^2) + 2ic_{s0}^2 k_{zr}k_{zi} + ig\gamma k_{zr} - g\gamma k_{zi}\right]\omega^2 + (\gamma - 1)g^2k_x^2 = 0 \quad (2.18)$$

Searching solutions for the imaginary part:

$$2c_{s0}^2 k_{zr}k_{zi} + g\gamma k_{zr} = 0 \quad (2.19)$$

$$k_{zi} = -\frac{\gamma g}{2c_{s0}^2} = -\frac{\gamma g \rho_0}{2\gamma P_0} = -\frac{g\rho_0\mu}{2\rho_0 R T_0} = -\frac{1}{2H} \quad (2.20)$$

Where μ is the atomic mass per particle, R is the ideal gas constant, T is the temperature, and H is the pressure-scale height.

The vertical wavenumber has the following form:

$$k_z = k_{zr} - \frac{i}{2H} \quad (2.21)$$

The solutions proposed for the velocity transform as:

$$\vec{v} \sim exp(ik_z z) = exp(ik_{zr}z + \frac{z}{2H}) \quad (2.22)$$

As we can see Eq. 2.22 can be split into two term: one defining the amplitude of the waves $e^{\frac{z}{2H}}$ and one defining the oscillatory motion $e^{ik_{zr}z}$. The amplitude term is always positive for $z > 0$. This mean that as z increases the amplitude of oscillations must increase also, proving the third point presented before.

Now we will define two important frequencies that will be useful for the following procedure.

- Acoustic cut-off frequency:

$$\omega_c = \frac{c_{s0}}{2H} = \frac{\gamma g}{2c_{s0}} \quad (2.23)$$

- Brunt-Väisälä frequency:

$$N^2 = g\Big[\frac{1}{\gamma P_0}\frac{dP_0}{dz} - \frac{1}{\rho_0}\frac{d\rho_0}{dz}\Big] = g\Big[-\frac{1}{\gamma H} + \frac{1}{H}\Big] = \frac{g}{H}\frac{(\gamma-1)}{\gamma} \tag{2.24}$$

Searching for solutions for the real part of Eq. (2.18), using this defined frequencies we arrive at the following dispersion equation:

$$\omega^4 - \omega^2(c_{s0}^2(k_x^2 + k_{zr}^2) + \omega_c^2) + N^2 c_{s0}^2 k_x^2 = 0 \tag{2.25}$$

Solving for k_{zr} one obtains:

$$k_{zr}^2 = \frac{(\omega^2 - \omega_c^2)}{c_{s0}^2} + \frac{k_x^2}{\omega^2}(N^2 - \omega^2) \tag{2.26}$$

For our study, where all waves propagate vertically, we consider $k_x = 0$ and we obtain:

$$k_{zr} = \pm\frac{\sqrt{(\omega^2 - \omega_c^2)}}{c_{s0}} \tag{2.27}$$

Using this results, the solutions proposed are of the following form:

$$v_z(z,t) = A(z)e^{\frac{z}{2H}}e^{i(\pm\sqrt{(\omega^2-\omega_c^2)}/c_{s0} - \omega t)} \tag{2.28}$$

From Eq. 2.28 we can define two different behaviour depending on the value of ω. If $\omega > \omega_c$, k_{zr} will take real values and there will be propagation. If instead $\omega < \omega_c$, k_{zr} will be imaginary, and the phase of the wave will depend only of time. In this case, for all z waves are in phase and are evanescent.

2.3 Acoustic-gravity waves with radiative losses.

Now we will relax the adiabatic condition and letting the fluid to have radiative losses with a Newton's cooling law ($Q_{rad} = -c_v\frac{\Delta T}{\tau_r}$). Also we will consider the effects of gravity. We obtain different results from the adiabatic case but in form they are similar.

Taking into account that Newton's cooling law damps temperature fluctuations, with a typical relaxation time τ_r given by:

$$\tau_r = \frac{\rho c_v}{16\chi\sigma_R T^3} \tag{2.29}$$

where c_v is the specific heat per unit volume, χ is the mean absorption coefficient and σ_R is the Stefan-Boltzmann constant.

The system of equations (2.10) in non-adiabatic case is maintained the same, except for the energy conservation equation. The energy conservation equation takes the following form:

$$\frac{\partial}{\partial t}\left(\rho\epsilon+\rho\frac{v^2}{2}\right)=-\vec{\boldsymbol{\nabla}}\left[(\rho\frac{v^2}{2}+\rho\epsilon+P)\vec{v}\right]+\vec{g}\cdot\vec{v}-c_v\frac{\Delta T}{\tau_r} \tag{2.30}$$

Introducing solutions like those found for the adiabatic case:

$$v_z=A(z)e^{z/(2H)}e^{ik_z z} \tag{2.31}$$

We obtain the following dispersion relation:

$$k_z^2=\frac{\omega^2-\hat{\omega}_{ac}^2}{\hat{c}^2} \tag{2.32}$$

where

$$\hat{\omega}_{ac}=\frac{\hat{c}}{2H},\qquad \hat{c}^2=\hat{\gamma}gH,\qquad \hat{\gamma}=\frac{1-i\gamma\omega\tau_r}{1-i\omega\tau_r} \tag{2.33}$$

As we can see, k_z is a complex number, computing the real and imaginary parts one obtains:

$$k_R^2=\frac{1}{2}\Big[h_R+(h_R^2+h_I^2)^{1/2}\Big] \tag{2.34}$$

$$k_I^2=\frac{1}{2}\Big[-h_R+(h_R^2+h_I^2)^{1/2}\Big] \tag{2.35}$$

where

$$h_R=\frac{\omega^2(1+\omega^2\tau_R^2\gamma)}{gH(1+\omega^2\tau_R^2\gamma^2)}-\frac{1}{4H^2} \tag{2.36}$$

$$h_I=\frac{\tau_R\omega^3(\gamma-1)}{gH(1+\omega^2\tau_R^2\gamma^2)} \tag{2.37}$$

2.4 Effects of gravity and radiative losses on wave propagation

Figure 1 shows the theoretical phase difference spectra between two heights of the solar atmosphere obtained under different assumptions. Acoustic waves in an homogeneous fluid are free to propagate in all directions regardless of their frequency (black solid line). In contrast, when we take into account the gravity in the adiabatic approximation theoretical model, an acoustic cut-off frequency appears. This cut-off frequency defines the minimum value for the frequency of oscillations to be able to propagate (black dashed line).

If we consider the effects of radiative losses, there is not a strict cut-off frequency and waves with all frequencies can partially propagate. However, a pseudo-cutoff frequency can be de-

fined. This pseudo-cutoff frequency takes lower value than the cut-off frequency in the adiabatic limit (green dashed-dotted line).

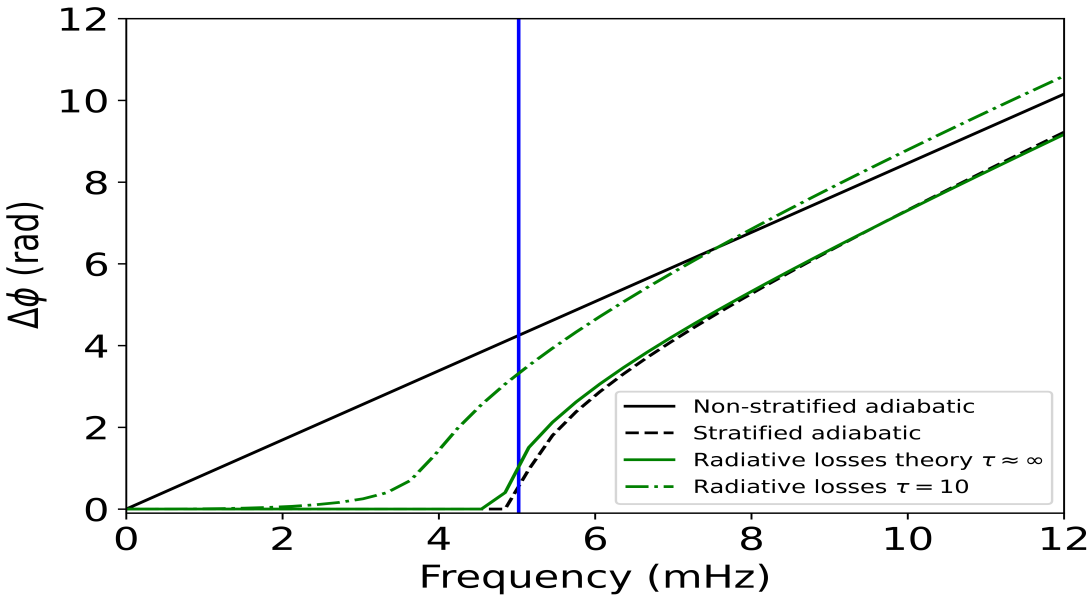

Figure 1: Phase difference spectrum comparing three theoretical models of wave propagation between two layers of the solar atmosphere with a height difference of 1000 km. Blue: Mean value of the acoustic cut-off frequency for these regions.

2.5 Resonant cavity model theory

We will present a brief introduction on the theoretical background of the resonant cavity model. In this model, upward propagating waves can reflect at the transition region. This reflection is due to the steep temperature gradient.
In the chromosphere, there is a mixture of upward and downward propagating waves. This mixture induces the formation of standing waves. These waves are characterized for being stationary (they oscillate in time but the locations of their peak amplitudes do not move in space). The location of the amplitude minimums are called nodes, and the locations where the absolute value of the amplitude is maximum are called antinodes.

The location of the nodes depends on the frequency of the oscillations. In a simple model, like an organ pipe, the positions of the velocity nodes are [16]:

$$h = \frac{2n-1}{4}\frac{c_{s0}}{\nu}, \qquad n = 1, 2, 3, ... \tag{2.38}$$

where h is the height from the transition region, c_{s0} is the sound speed of the layer studied (for our study it will be the chromosphere), and ν is the frequency of the oscillations.

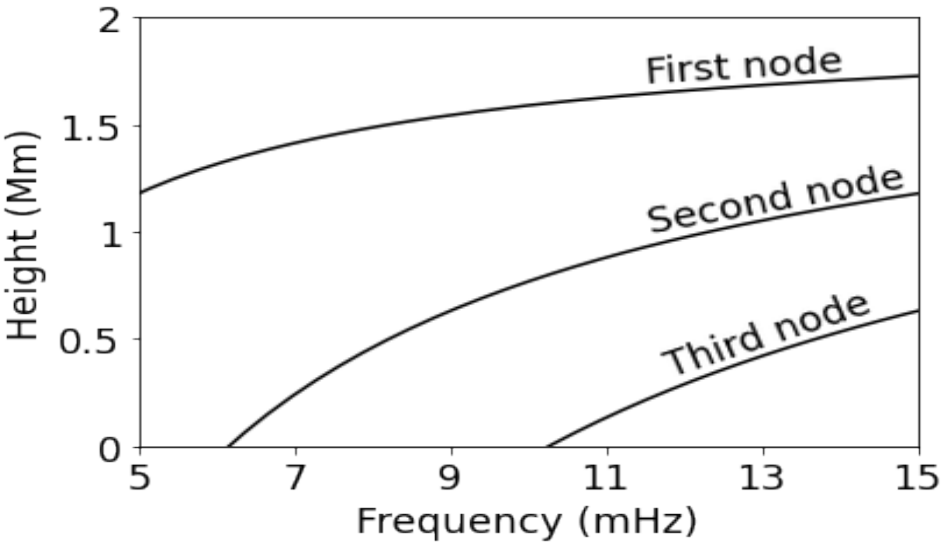

Figure 2: Height position of the velocity oscillations nodes as a function of frequency in a simple model of a resonant cavity produced by frequency-independent reflections at z=2000 km.

Figure 2 illustrates how the position of the nodes varies with the frequency of the oscillations. The position of the different nodes approaches the reflective layer (transition region, $z \approx 2000$ km) as the frequency increases.

Velocity oscillations at opposite sides of a node exhibit a π rad phase difference. The detection of these phase jumps can be employed to confirm the resonant nature of the oscillations and to locate the presence of the nodes. According to this model, at the positions of the nodes (taking into account their height and frequency) a lower oscillatory power is expected.

3 Numerical simulation

In this section we will present details on the simulation used to obtain the results presented in this work.

The code used to solve the ideal MHD equations is called MANCHA [17] [18]. This simulation used a 2.5D approximation, employed a 2D domain for the computations but kept all the vectors with 3D coordinates.
The code solves non-linear equations. Since umbral flashes, as we commented in the introduction, form shock waves.
Wave propagation has been computed from below the photosphere to the corona in the umbral model M from [19] with 2000 G vertical magnetic field.

As we said before the simulation worked in the adiabatic limit, where no radiative energy transfer was considered, and so the simulation have the following properties:

- Vertical domain going from $z = -1140$ km to $z = 3500$ km, where $z = 0$ is set at the height where the optical depth at 5000 Å is unity ($log\ \tau = 0$). The interval considered is constant through all the domain with $dz = 10$ km.
- Horizontally it has a domain going from $x = 0$ km to $x = 4800$ km with a total of 96 points and a horizontal step $dx = 50$ km.
- At the top and bottom boundaries a perfectly matched layer was imposed, to damp waves with minimum reflection.
- In the horizontal direction periodic boundary conditions were imposed.
- Temporal step of $dt = 12\ s$ with a total of 276 time steps.
- A total of 55 minutes of solar time were computed, and the whole interval was used for the calculations.

A vertical force in $z = -180$ km drives the waves, this force was derived from sunspot observations [18] [20]. From this simulation we obtained the following variables used for the study:

- Height: z
- Pressure: P
- Density: ρ
- Temperature: T
- X-direction magnetic field: B_x
- Z-direction magnetic field: B_z
- Horizontal velocity: v_x
- Vertical velocity: v_z

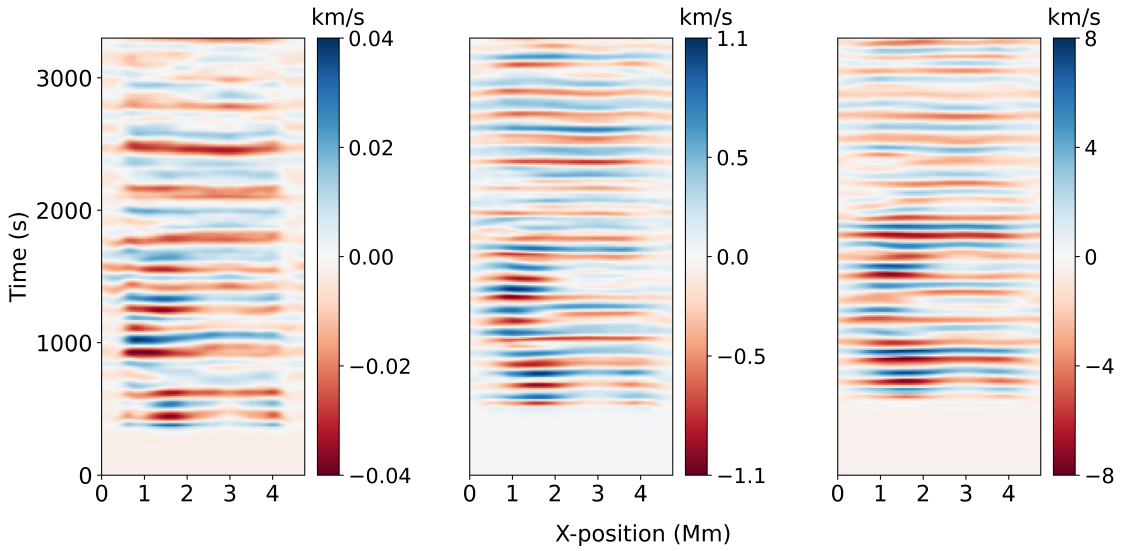

Figure 3: Temporal evolution of the vertical velocity at z = 340 km (left panel), z = 1200 km (middle panel), and z = 2000 km (right panel). Positive velocities (blue) correspond to upflows.

In Figure 3 we are showing vertical velocity, the data is obtained from the simulation. From this figure it is easy to see the formation of waves in the alternating pattern of the velocity, the typical oscillatory behaviour expected from waves. Inspecting the figure one can see that at higher atmospheric layers the amplitude of the oscillations increases orders of magnitude, so as we said in the introduction, shock formation at chromospheric layers is a common phenomena.

The height where we represent the slices was determined using as reference the average heights of formation of different spectral lines. In particular approximately at z=340 km the Si I 10827 line is formed, at z = 1200 km the Ca II 8542 is created and at z = 2000 km the He I 10830 line is formed.

From all this data we can determine the principal characteristics of the atmosphere simulated. In particular we will determine:

- Sound speed: $c_{s0} = \left(\frac{\gamma P_0}{\rho_0}\right)^{1/2}$
- Alfvén speed: $v_A = \frac{B_0}{(\mu_0 \rho_0)^{1/2}}$
- Plasma-beta: $\beta = \frac{c_{s0}^2}{v_A^2}$
- Acoustic cut-off frequency: $\omega_c = \frac{c_{s0}}{2H} = \frac{\gamma g}{2c_{s0}}$
- Pressure scale height: $H = \frac{c_{s0}^2}{\gamma g} = -\frac{P}{\left(\frac{dP}{dz}\right)}$

In the simulation the gravity g is considered constant through all the 2D domain with a value of $g = 274\ ms^{-2}$, the parameter γ is the ratio between specific heats, in this case where a ideal fluid is supposed it has a value of $\gamma = \frac{5}{3}$ and finally the parameter μ_0 is the magnetic permeability of the vacuum $\mu_0 = 4\pi \cdot 10^{-7} N/A^2$.
All the variables with a 0 sub-index refer to the initial conditions, as we said in the latter chapter.

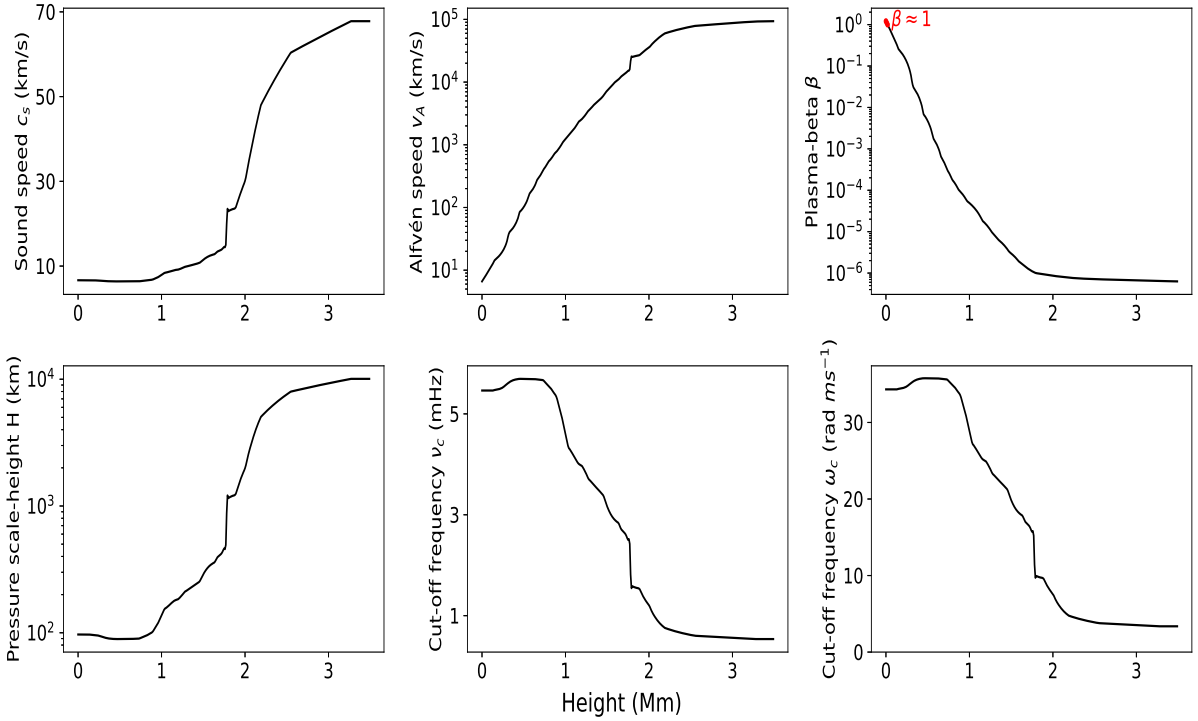

Figure 4: Parameters obtained from the simulation for the height greater than zero.

From Figure 4 we can analyze how the waves propagate through the whole atmosphere.

First of all, as we can see from the plots of the characteristic velocities, c_{s0} and v_A, drastically increase with height.

We highlighted by red the location where the plasma-beta takes a value of approximately 1. Waves at $z \approx 0$ propagate at different speeds, depending on their mode (slow or fast

magnetoacoustic or Alfvén) and on their direction. At upper layers the Alfvén speed starts dominating over the sound speed. At chromospheric and higher layers, the velocity of propagation of slow magnetoacoustic waves (given by the sound speed) compares to the amplitude of the velocity oscillations (see Figure 3). This explain the shock formation in this layers.

Knowing the pressure scale-height, we also know the temperature of the atmosphere:

$$H = \frac{c_{s0}^2}{\gamma g} = \frac{\gamma P_0}{\rho_0}\frac{1}{\gamma g} = \frac{P_0}{\rho_0 g} = \frac{\mathcal{R}T}{\mu g}; \qquad H \propto T \tag{3.1}$$

Where $\mathcal{R}$ is the ideal gas constant, and μ is the atomic mass per particle.
The largest temperature gradient we observe is situated at the transition region where waves can be reflected. The existence and consequences of this layer will be analyzed in the following chapter.

Finally, as we can see from the last two plots, the cut-off frequency reduces its value at higher layers of the atmosphere. The cut-off frequency is a parameter that tells us which wave modes can propagate through the atmosphere. All the waves with frequency lower than the cut-off dissipate and cannot propagate, in contrast all the waves with higher frequency propagate through the atmosphere. One can observe that due to decrease of the cut-off frequencies, waves with lower frequencies are able to propagate at higher layers. This happens thanks to the increase of temperature in the transition region into corona.

4 Wave analysis

In this section, we will present the Fourier analysis of the waves we studied from the simulation. We will fit the data obtained to the different wave propagation models and analyze the resonant cavity model.

4.1 Fourier Analysis

Fourier analysis is the method used to analyze wave propagation in this work. In particular, we did the Fast Fourier Transform (FFT) of the 2D velocity map. From this FFT we can obtain the power spectrum and phase spectrum of the waves at different heights.

From the FFT we obtain an array of Fourier coefficients [1].

- Taking the squared absolute value of the coefficients, we obtain the power spectrum: $A = FFT(a) \rightarrow Power = |A|^2$
- The coefficients are complex numbers with real and imaginary part, we can obtain the phase of the Fourier harmonics with the standard procedure, and obtain this way the phase spectrum. $\Phi = \arctan\left(\frac{Im(z)}{Re(z)}\right)$ and then unwinding it's range to $\Phi \in [-\pi, \pi]$.

We will begin presenting the results of the Fourier analysis for oscillations in the photosphere and the chromosphere. We will show both power and phase difference spectra and explain the results obtained.

Then we will show the fits we did. We fitted the results to the theoretical model with radiative losses presented in Chapter 2.3. Two types of independent fits were made: Amplification fits and Phase difference fits.
Each of these fits has been performed for the spectra computed between two layers with a large height difference ($dz = 1000$ km) and a fine study with $dz = 200$ km.

Finally, we will present the phase difference spectra for different pairs of variables at the same height. Since a detailed study of this results is out of scope for this work, we will not focus out attention in it.

4.2 V-V spectra

In this section we will present the power and phase difference spectra we obtained from the data. We will begin presenting a comparison between the photospheric and chromospheric oscillations, explaining the results obtained.

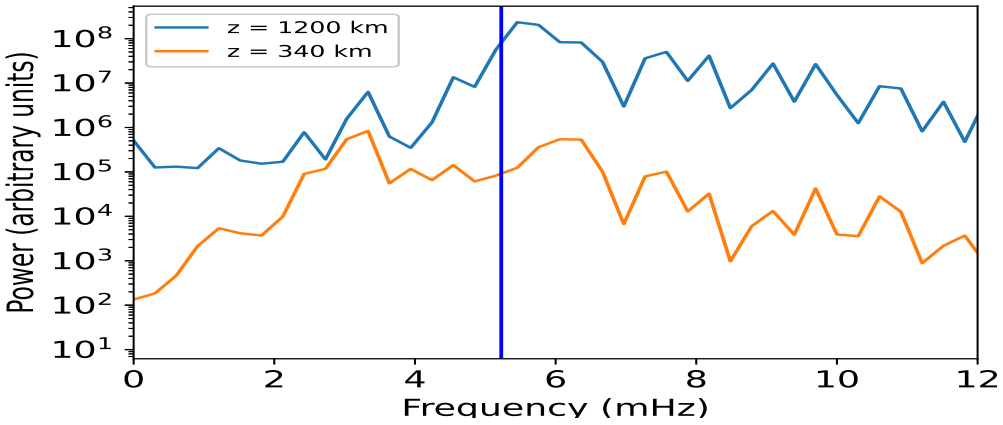

Figure 5: Power spectrum at the photosphere and the chromosphere, heights used are determined by different spectroscopic line formation. The vertical line situated around 5 mHz is the cut-off frequency in this region.

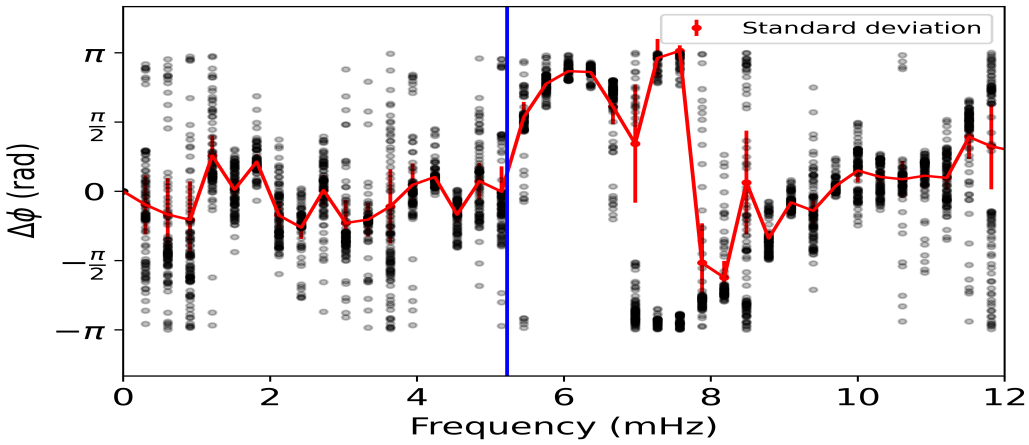

Figure 6: Phase difference spectrum of the velocity of the propagating waves at the photosphere in comparison to the chromosphere (340 - 1200 km). The black points represent the values in all x for the phase difference, red line is the mean values of the phase difference with error bars represented by the standard deviation of the values.The vertical line situated around 5 mHz is the cut-off frequency is the mean value in this region.

From Figure 5 we can see the velocity wave power spectra for the photospheric and chromospheric heights. As one can see, the main modes are located in the two frequency regions:

3 mHz (5-min) for the photospheric oscillations and 5-6 mHz (3-min) for the chromospheric oscillations.
The power of the oscillations increases with height. As we said shock formation is a common phenomena in the chromosphere, so the expected power must be higher than in the photosphere.

Also for the chromosphere, the main mode of propagation is around the acoustic cut-off frequency calculated. This can be explained since waves with frequencies below the cut-off cannot propagate to the chromosphere. Only oscillations with frequencies above the cut-off propagate through the atmosphere and arrive to the chromosphere.

Figure 6 shows the velocity phase difference spectra between the photospheric and chromospheric velocity oscillations. Oscillations with frequencies below the cut-off, as previously said, cannot propagate through the atmosphere. In this spectrum, this behaviour can be identified by the 0 phase difference. As we consider frequencies above the cut-off frequency, the phase difference increases. The progressive increase of the phase difference with frequency indicates that there is wave propagation between these two atmospheric layers.

4.3 Fits and wave propagation model comparison

In this section, we will present a comparison between the three theoretical models of the wave propagation presented in Chapter 2 and the actual measurements from the numerical simulation. Since we already know our data comes from an adiabatic simulation of a sunspot, we expect the adiabatic limit to present the best results when compared to the data.
The study was made via the fitting of the data obtained by the simulation, treating it like it was observational data. We fitted to the theoretical model with radiative losses. One of its limits is the adiabatic case (see Appendix 1). We independently fitted two quantities: the amplification spectra and the phase difference spectra measured between the velocity oscillations at two different heights. In addition, we know the actual atmospheric stratification from the atmosphere, so we can compute the spectra expected if wave propagation is assumed.

From these fits we obtain three free parameters: Height difference (dz), relaxation time (τ_r), and pressure scale-height (H). Since we already know the simulation was adiabatic we expect to obtain huge values of τ_r for each fit. The height difference is a parameter we know with total accuracy, since we impose it, and it will help us determine the validity of the fits. The pressure scale-height can also be obtained from the numerical simulation data and can be seen in Figure 4.

The objective of these fits is to analyze the wave propagation through two big sections of the atmosphere: photosphere-chromosphere and chromosphere-transition region. We will do fine analysis in intervals of 200 km. The comparison of the numerical simulations measurements with the analytical modelling will provide information about the nature of the umbral oscillations. The employed analytical models do not take into account the standing oscillations produced by the presence of a resonant cavity. Thus, the discrepancies between theory and simulation can provide some insights about the atmospheric layers where the wave reflections at the transition region impact wave propagation.

4.3.1 Photosphere-chromosphere fits

We will present the results for the photosphere to the chromosphere. The following analysis spans from 340 km to 1340 km of the solar atmosphere.

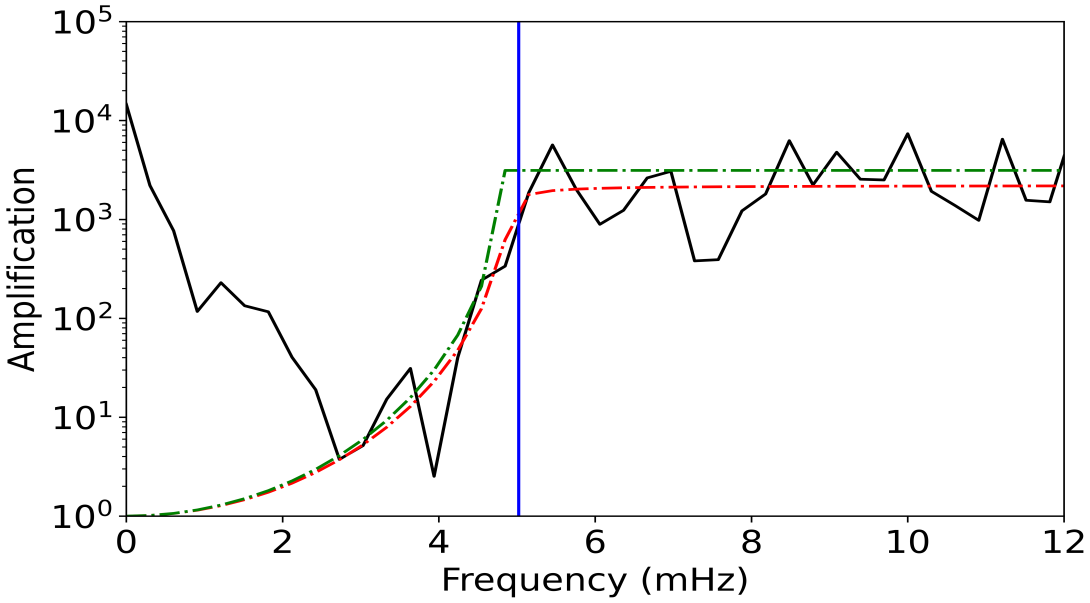

Figure 7: Amplification spectra between z = 340 km and z = 1340 km. Black line: Data from the simulation. Green line: Theoretical prediction using the known atmospheric values for the three free parameters. Red line: Fit. Blue line: Mean value of the acoustic cut-off frequency for this region.

Figure 7 shows the different behaviour of waves in two regions of the spectrum. From 2 to 5 mHz the amplitude of the chromospheric waves progressively increases. Above the cut-off frequency we can see how the amplification spectra shows a huge increment. Waves from this frequency region can freely propagate to the chromosphere. Since kinetic energy must

be conserved and the chromosphere has a reduction in density, the amplitude of velocity oscillations must increase.
The results predicted by the theory exhibit a remarkable agreement with those obtained from the fits.

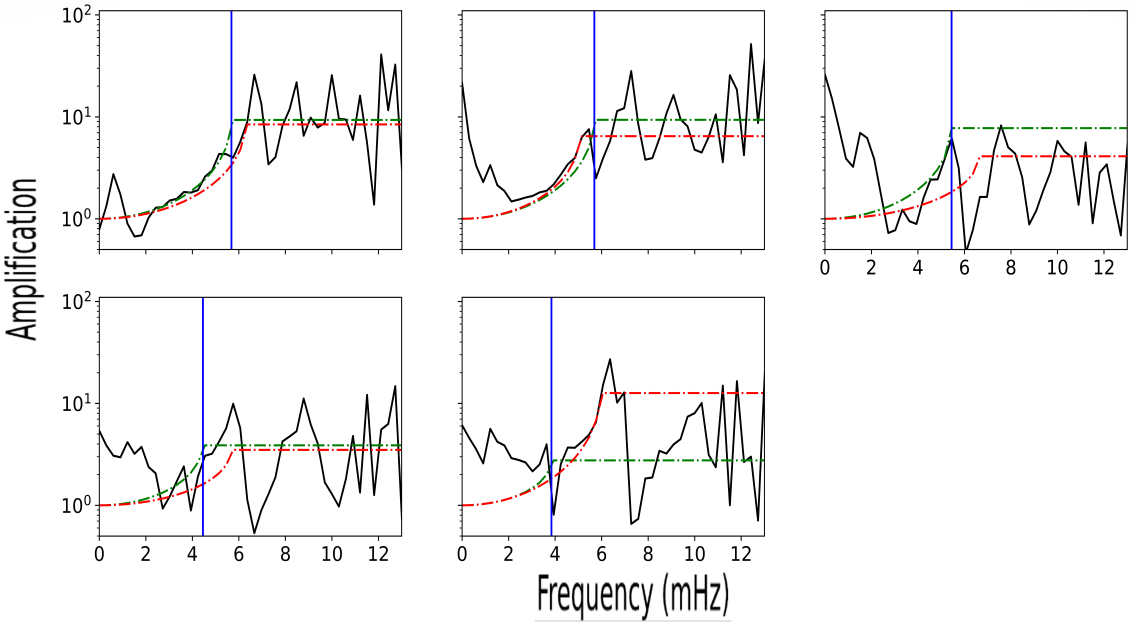

Figure 8: Amplification spectra with a height difference $dz = 200$ km. Lines have the same meaning as in Figure 7. Top left: $340 - 540$ km, Top center: $540 - 740$ km, Top right: $740 - 940$ km, Bottom left: $940 - 1140$ km Bottom center: $1140 - 1340$ km.

Figure 8 illustrates the amplification spectra in the same atmospheric region, but analyzing smaller height differences between oscillatory signals. The behaviour shown in Figure 7 repeats. The theory predictions and the fits match the trends in some cases, but with lower confidence than in Figure 7. Also, some dips in amplification are found at the higher layers of the study (940-1340 km). These sudden reductions in amplification indicate that there probably is a mixture of upward and downward propagating waves.

Figure 9 shows the phase difference spectra for waves between 340 and 1340 km. Similar to the amplification spectra, there are two separate regions delimited by the acoustic cut-off frequency of this region. Below 5 mHz, waves are generally in phase, i.e. 0 phase difference (see red and green lines). Above this mark, phase difference increases with frequency. Both the theoretical prediction and the fit agree with this results.

Results from Figure 10 generally match those presented in Figure 9. They also show an increase in the phase difference with frequency. However, there are sudden bumps in phase difference. The frequency of these bumps match the reduction in amplification spectra, confirming the presence of resonant nodes. At the nodes, the amplitude of the oscillations is minimum (and, thus, there are dips in the amplification spectra at their locations, see Figure 8), and phase

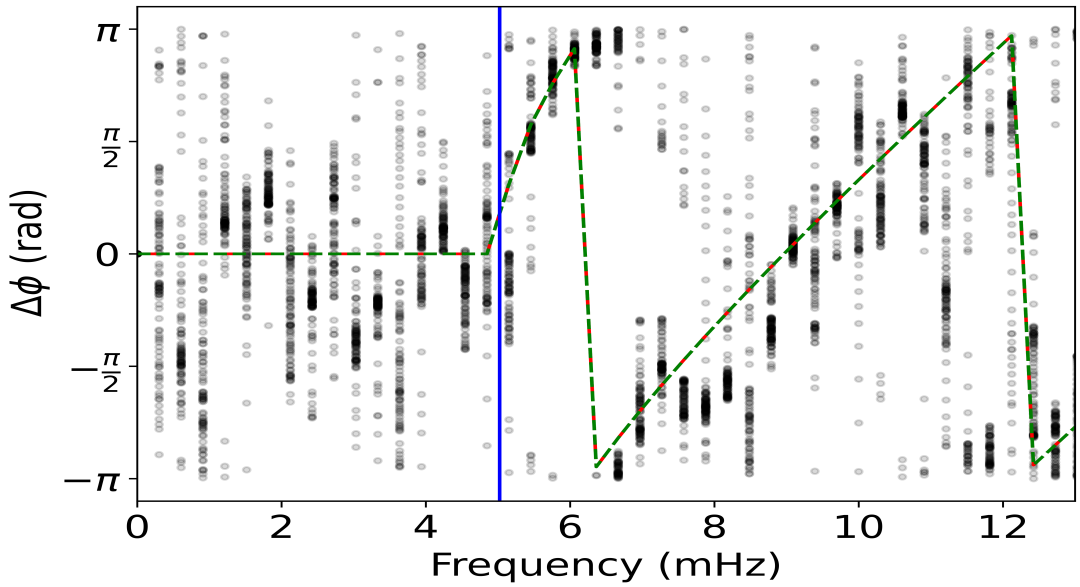

Figure 9: Phase difference spectra between z = 340 km and z = 1340 km. Black dots: Data from the simulation. Green, red, and blue lines have the same meaning as in Figure 7.

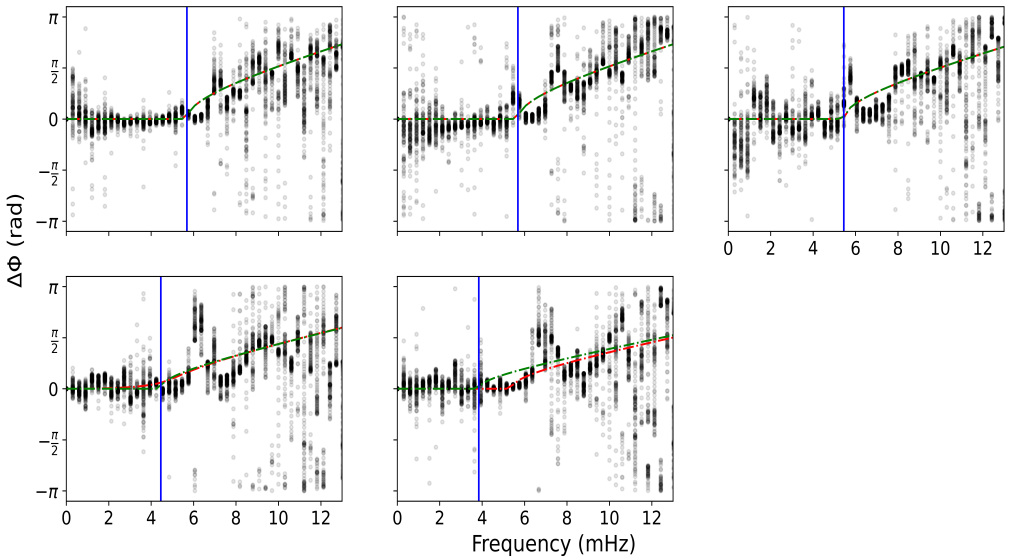

Figure 10: Phase difference spectra with a height difference $dz = 200$ km. Lines have the same meaning as in Figure 7. Top left: $340 - 540$ km, Top center: $540 - 740$ km, Top right: $740 - 940$ km, Bottom left: $940 - 1140$ km Bottom center: $1140 - 1340$ km.

jumps are produced (Figure 10).

The location of these bumps moves to higher frequencies as we increase the height of the analysis. The existence of the bumps in phase difference is one of the predictions of the res-

onant cavity model, as well as, the translation to higher frequencies with height (see Figure 2).

We can conclude that in this region wave propagation takes place. Slow magneto-acoustic waves start at the photosphere and travel to the chromosphere following the magnetic field lines. The results predicted by the theoretical model of wave propagation match the measurement from the simulation. However, the model fails in the region $940 - 1340$ km, where jumps in phase difference and dips in the amplification are found. They point to a mixture of propagating and standing waves in this region.

4.3.2 Chromosphere - transition region fits

In this section, we present the results for the upper region studied, which spans from 1340 km to 2340 km of the solar atmosphere. We will repeat the same structure employed for the presentation of results from the photosphere-chromosphere region.

The nature of the oscillations will be evaluated from the examination of the phase and amplification spectra computed from the simulation and their comparison with the theoretical model of wave propagation. We will evaluate if stationary waves are formed in this region via the reflection of incident waves at the transition region (where there is a steep temperature gradient). The formation of standing waves can be determined by sudden jumps of π rad in phase difference. These sudden increases in phase difference occur when the heights studied are in different regions of the standing wave determined by the nodes. We should also expect a displacement of the nodes to higher frequencies as we increase the height, and a reduction of the wave amplitude at the nodes.

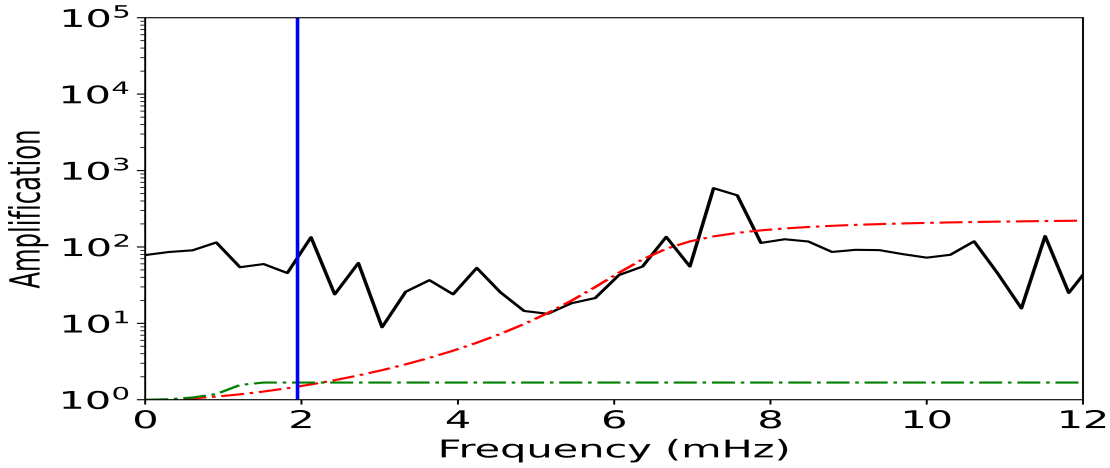

Figure 11: Amplification spectra between z = 1340 km and z = 2340 km. Lines have the same meaning as in Figure 7.

Figure 11 shows the amplification spectra for waves at the chromosphere and the transition region. As we can see, standard wave propagation models cannot predict the results obtained. We see a general trend of an amplification of two orders of magnitude for all frequencies.

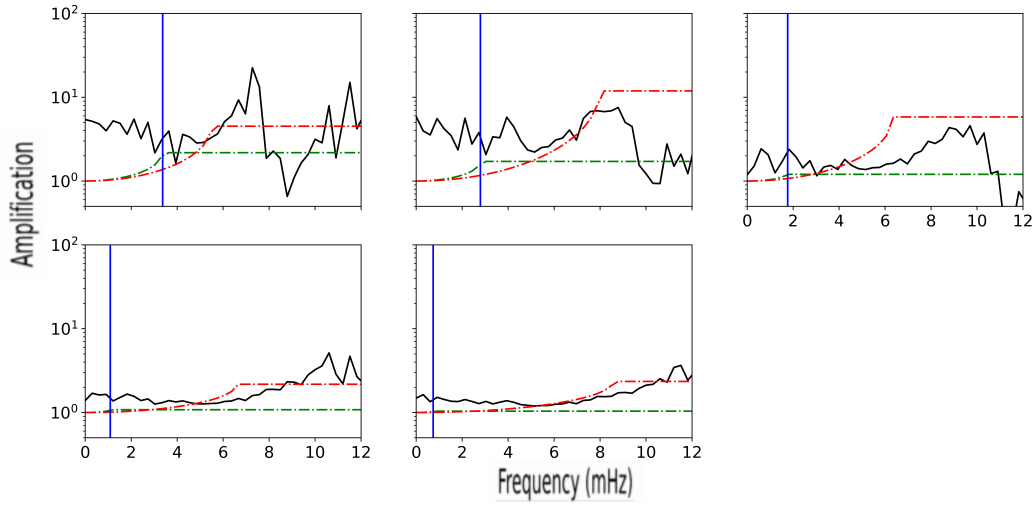

Figure 12: Amplification spectra with a height difference $dz = 200$ km. Lines have the same meaning as in Figure 7. Top left: $1340 - 1540$ km, Top center: $1540 - 1740$ km, Top right: $1740 - 1940$ km, Bottom left: $1940 - 2140$ km Bottom center: $2140 - 2340$ km.

Figure 12 shows the amplification spectra obtained for intervals of 200 km. Theoretical predictions (green lines) and fits (red lines) assuming a model of wave propagation cannot reproduce the measurements from the simulation (black line). Significant dips in the amplification are found at specific frequencies. They are shifted to higher frequencies as higher layers are considered.

Figure 13 also shows that wave propagation models cannot predict the results obtained from the simulation. The phase difference spectrum exhibits a π rad jump between 7 and 8 mHz. This behaviour does not match the adiabatic wave propagation, where a progressive increase in phase difference is expected above the acoustic cut-off frequency.

Figure 14 shows the phase difference spectra between the velocity signals from two layers with a lower height difference, all of them from the upper atmosphere. We find the presence of sudden bumps in the spectra. These bumps are around $\pi/2$ radians. The resonant cavity model predicts increases of π radians. The increments we find in phase difference do not match the expected values. This is due to the short atmospheric height difference chosen for the plots (dz=200 km). In the simulation, the π rad jump at the nodes takes places progressively. As we go from lower to higher frequencies, the lower atmosphere first reach the velocity node (Figure 2). In the range of frequencies where the lower and upper heights considered are at different sides of the node, a phase difference jump is present. However, both

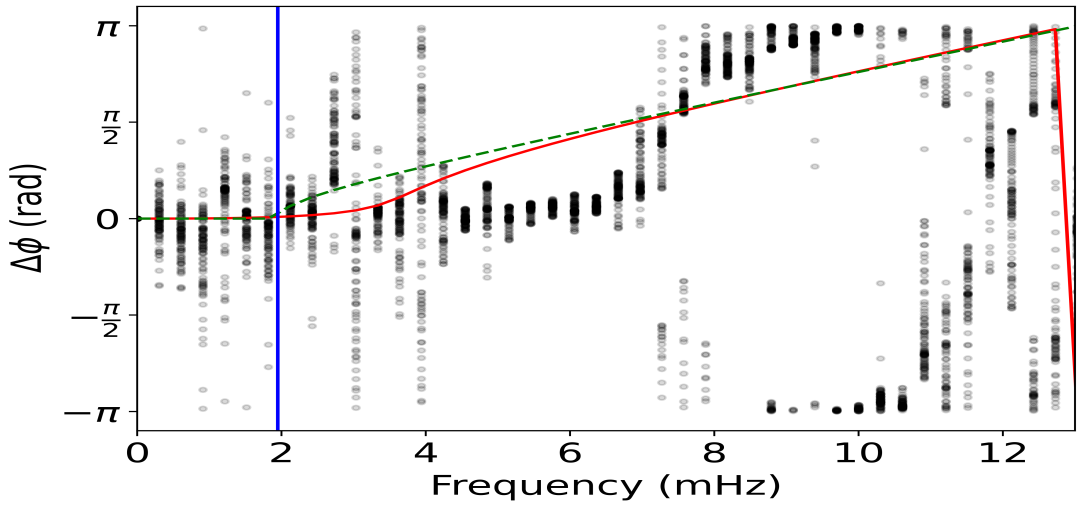

Figure 13: Phase difference spectra between z = 1340 km and z = 2340 km. Black dots: Data from the simulation. Green, red, and blue lines have the same meaning as in Figure 7.

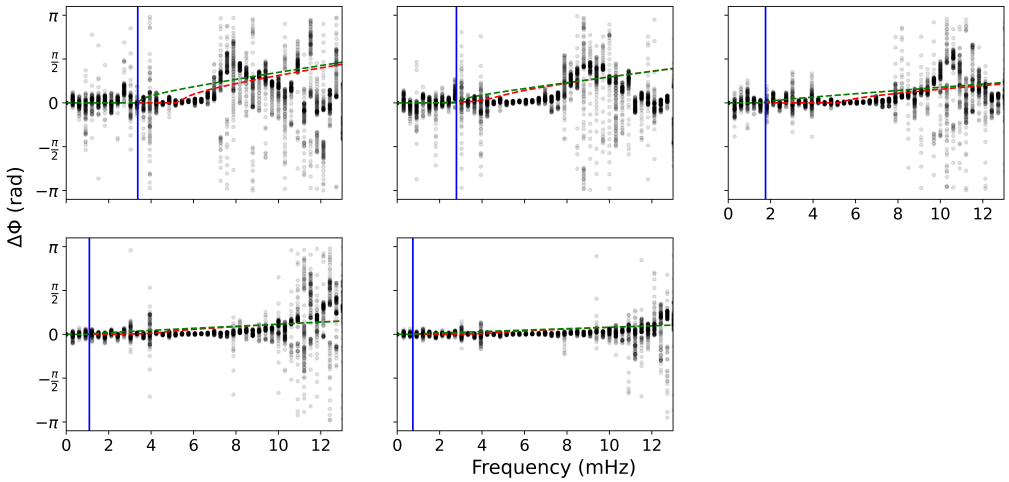

Figure 14: Phase difference spectra with a height difference $dz = 200$ km. Lines have the same meaning as in Figure 7. Top left: $1340 - 1540$ km, Top center: $1540 - 1740$ km, Top right: $1740 - 1940$ km, Bottom left: $1940 - 2140$ km Bottom center: $2140 - 2340$ km.

heights are again at the same side of the node before the full π rad jump is found in the spectra.

Our results are in agreement with the behaviour of the chromospheric resonant cavity model. The expected jumps in phase difference are shown in Figure 14, with the corresponding shift of them to higher frequencies as the height increases (see Figure 2).

The π rad bumps in phase difference predicted by the chromospheric resonant cavity model

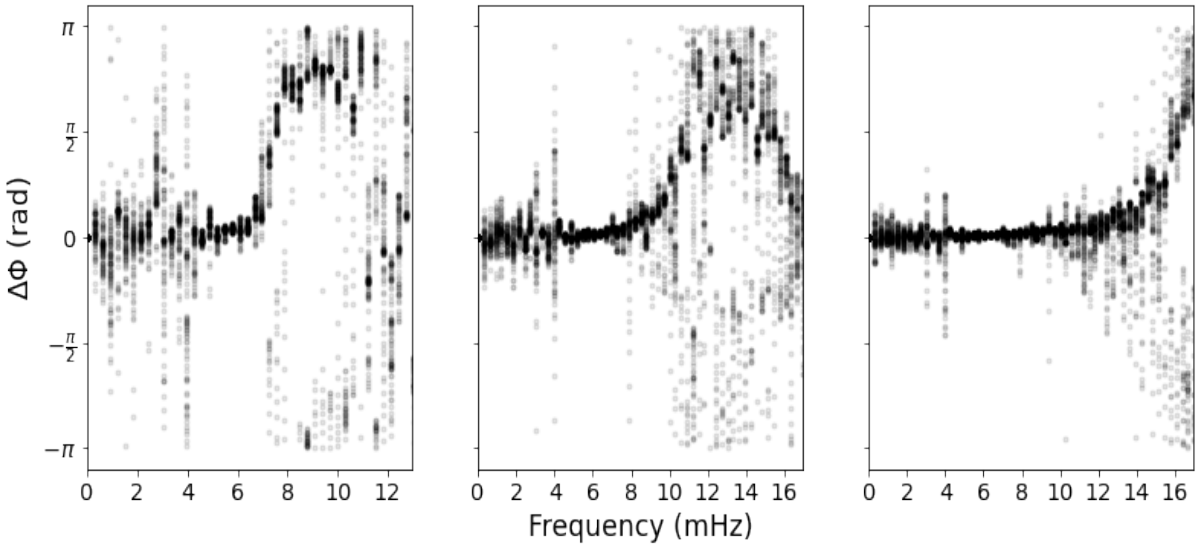

Figure 15: Phase difference spectra of higher layers of the solar atmosphere with $dz = 500$ km. Left: $1340 - 1840$ km, Center: $1840 - 2340$km, Right:$2340 - 2840$km

appear clearly in Figure 15. In this case, the height difference for the calculations is large enough so waves can develop a full π radians phase shift. The spectrum from the left panel is restricted to lower frequencies since the results are noisier and the return to 0 phase difference cannot be clearly seen.

These results show that, at the upper chromosphere of the simulation, oscillations cannot be interpreted as propagating waves. The fits do not match the results (black lines), and their shapes differ from the expected behaviour. We can conclude that a resonant cavity exists in this region of the sunspot and standing waves are formed.

Finally, we present the parameters obtained from the different fits in Tables 1 and 2. The actual values of the three free parameters are known from the simulation. Since it was computed in the adiabatic regime, the radiative cooling time is infinite. The height difference was chosen for the computation of the spectra, and the pressure scale height can be computed from the atmospheric stratification (Figure 4). This way, we can evaluate how well the model of wave propagation can explain the measurements from the simulation.

Table 1 shows a good agreement between the values of the fits and the expected parameters. The fits recover with reasonable success the height difference (either 1000 or 200 km), the pressure scale height (slightly below 100 km), and a extremely high relaxation time, as expected from adiabatic wave propagation.
On the contrary, the theoretical model of wave propagation does not characterize the oscilla-

	dz (km)	H (km)	τ_r (s)
Amp. fit, dz = 1000 km	932.7	119.8	550.0
Amp. fit, dz = 200 km	155.4 211.6 92.7 112.4 207.8	72.9 113.4 65.6 89.8 81.9	$3.2 \cdot 10^9$ $9.2 \cdot 10^8$ $8.1 \cdot 10^8$ $6.3 \cdot 10^8$ $5.0 \cdot 10^9$
Phase diff. fit, dz = 1000 km	932.7	119.8	549.9
Phase diff. fit, dz = 200 km	155.4 211.7 92.7 112.4 207.8	89.6 89.5 97.4 89.5 100.0	$4.4 \cdot 10^9$ $2.8 \cdot 10^8$ $6.4 \cdot 10^5$ $2.2 \cdot 10^1$ $1.5 \cdot 10^8$

Table 1: Parameters obtained for all the theoretical fits from the photosphere-chromosphere (340 km to 1340 km) layer of the simulation. The rows for fits with dz = 200 km are ordered downward, so the top results are for the sub-interval $340 - 540$ km, then $540 - 740$ km and so on.

	dz (km)	H (km)	τ_r (s)
Amp. fit, dz = 1000 km	409.1	64.7	19.1
Amp. fit, dz = 200 km	144.6 112.6 126.8 51.8 33.6	95.9 45.4 72.0 66.7 39.4	$4.1 \cdot 10^9$ $1.2 \cdot 10^9$ $7.8 \cdot 10^7$ $7.1 \cdot 10^8$ $5.8 \cdot 10^8$
Phase diff. fit, dz = 1000 km	320.3	150.0	18.0
Phase diff. fit, dz = 200 km	125.5 103.8 62.2 39.6 27.3	100.0 100.1 99.8 99.9 100.0	$9.9 \cdot 10^9$ $1.5 \cdot 10^1$ $1.0 \cdot 10^{10}$ $1.3 \cdot 10^1$ $1.3 \cdot 10^1$

Table 2: Parameters obtained for all the theoretical fits from the photosphere-chromosphere (1340 km to 2340 km) layer of the simulation. The rows for fits with dz = 200 km are ordered downward, so the top results are for the sub-interval $1340 - 1540$ km, then $1540 - 1740$ km and so on.

tions found in the upper chromosphere. As a result, the parameters obtained from the fits fail to predict their real values.

These results confirm that the presence of resonances is changing the wave propagation behaviour compared to the one predicted by the theoretical model.

4.4 Phase difference spectra between pairs of variables.

We have computed the phase difference spectra for pairs of variables obtained from the simulation, but taking both oscillatory signals at the same heights. This way one can appreciate the behaviour of different oscillations (pressure, density, velocity and temperature) in the photosphere and the chromosphere. Figure 16 shows all pairs of variables phase difference spectra

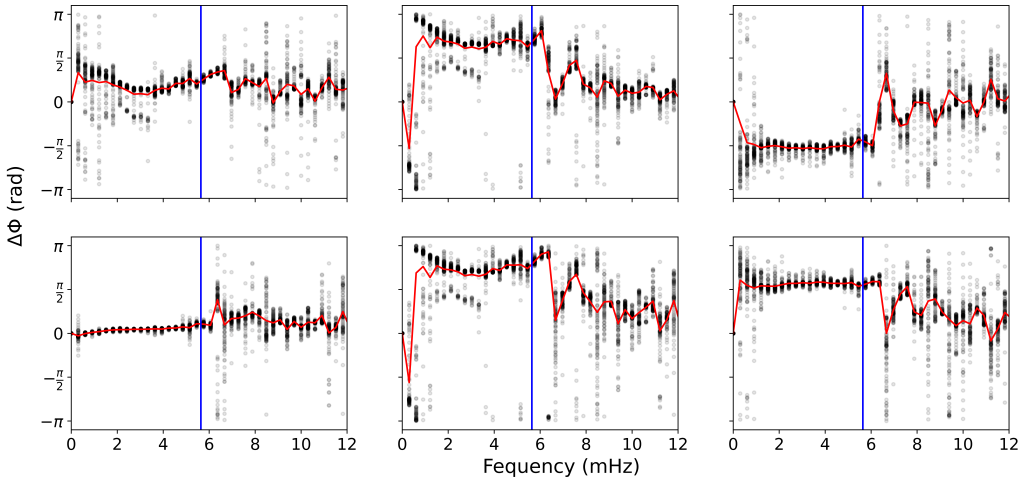

Figure 16: Phase difference spectrum at z = 340 km. Top left: T-Vz spectrum, Top center: T-P spectrum, Top right: P-Vz, Bottom left: P-ρ, Bottom center: T-ρ, Bottom left: Vz-ρ. Vertical lines show the acoustic cut-off frequency for z = 340 km

for oscillations at the same photospheric height. All of them exhibit a clear different behaviour for evanescent waves (frequency below 5 mHz) and for propagating waves (frequency above 5 mHz). The trend with frequency is increasing or decreasing depending of the pair of variables considered.

Figure 17 presents the same results as Figure 16, but at the low chromosphere (at approximately the formation height of the Ca II 8542 line). They show a complex dependence of the phase difference with the frequency, probably due to superposition of propagating and standing waves.

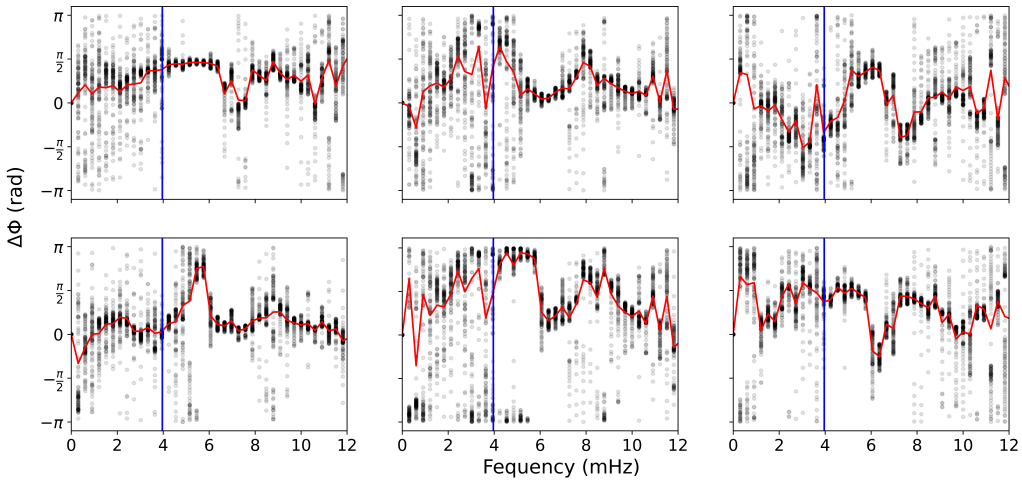

Figure 17: Phase difference spectrum at z = 1200 km. Top left: T-Vz spectrum, Top center: T-P spectrum, Top right: P-Vz, Bottom left: P-ρ, Bottom center: T-ρ, Bottom left: Vz-ρ. Vertical lines show the acoustic cut-off frequency for z = 1200 km

The study of these different phase difference spectra is out of scope for this work, so we will not focus our attention on it.

5 Discussion and conclusions

In this work, we have presented the results obtained from an adiabatic simulation of a sunspot. We studied wave propagation in it, obtaining the typical parameters that characterize the waves. We performed Fourier analysis, computing the Fast-Fourier Transform (FFT) of the different variables obtained from the simulation.

We studied mainly the velocity oscillations, centering our attention in one mode of propagation, slow magneto-acoustic waves. These waves travel through the photosphere to the chromosphere and upper layers. We analyzed three different theoretical models of wave propagation, in different limits: adiabatic without gravity, adiabatic stratified, and stratified with radiative losses.

The phase and amplification spectra between two atmospheric layers measured from the simulation were compared to those predicted by the analytical models. With this aim, we fitted the measurements from the simulation with a model of wave propagation in a stratifed atmosphere with radiative losses.
From the fits for the photospheric layers, we concluded that the results are consistent with wave propagation. These conclusions were extracted from the analysis of phase difference and amplification spectra. At the photosphere and low chromosphere oscillations with frequency below the acoustic cut-off frequency form evanescent waves, and cannot propagate freely to upper layers. Oscillations with frequencies above the acoustic cut-off have increasing phase difference with frequency, as the adiabatic model predicts.
For the upper chromosphere and transition region, we found that wave propagation cannot fit the data. One proposed model to explain this behaviour is the resonant cavity model, where the steep temperature gradient at the transition regions reflects incident waves, forming standing waves.

In this work, we concluded that a chromospheric resonant cavity model explains the behaviour of the oscillations in the upper umbral atmosphere. As we presented, theoretical models of wave propagation cannot describe correctly the phase and amplification spectra at the upper chromosphere. In the upper chromosphere, we have detected the presence of jumps in the phase difference spectra and dips in the amplification spectra, between velocity oscillations at different heights. These features are signatures of the presence of resonant nodes.

Phase jumps occur when the two heights are situated at different zones defined by nodes of the standing waves. As height increases the increments in phase difference move to higher frequencies. These bumps are predicted to be π rad. If the height difference between the considered atmospheric layers is large enough (≈ 500 km) they appear in the results of the simulation.

These jumps are predicted by the resonant cavity model [9] [10] [14] [15] [20], where standing waves are formed and the position of the nodes determines the locations where sudden phase shifts and reduced amplitudes are expected. The identification of these features confirms the standing nature of the umbral chromospheric oscillations in the simulation [16].

Bibliography

[1] Charles R. Harris, K. Jarrod Millman, Stéfan J. van der Walt, et al. "Array programming with NumPy". In: *Nature* 585.7825 (Sept. 2020), pp. 357–362. DOI: 10.1038/s41586-020-2649-2. URL: https://doi.org/10.1038/s41586-020-2649-2.

[2] E. Khomenko and M. Collados. "Oscillations and Waves in Sunspots." In: *Living Reviews in solar physics* 12.6 (2015).

[3] B. W. Lites. "Sunspot oscillations: observations and implications." In: *Sunspots: Theory and Observations, Cambridge, UK* (1992), pp. 261–302.

[4] A. S. Tanenbaum R. Howard and J. M. Wilcox. "A new method of magnetograph observation of the photospheric brightness, velocity, and magnetic fields". In: *Solar Phys.* 4 (1968), pp. 286–299.

[5] A. Wittmann. "Some Properties of Umbral Flashes". In: *Solar Phys.* 7 (1969), pp. 366–369.

[6] J. M. Beckers and P. E. Tallant. "Chromospheric Inhomogeneities in Sunspot Umbrae". In: *Solar Phys.* 7 (1969), pp. 351–365.

[7] H. Alfvén and B. Lindblad. "Granulation, Magneto-Hydrodynamic Waves, and the Heating of the Solar Corona." In: *Monthly Notices of the Royal Astronomical Society* 107 (1947), pp. 211–219.

[8] M. Schwazschild. "On Noise Arising from the Solar Granulation." In: *The Astrophysical Journal* 107 (1948).

[9] Y.D. Zhugzhda. "Seismology of a Sunspot Atmosphere." In: *Solar Phys.* 251 (2008), pp. 501–514.

[10] Y. D. Zhugzhda and V. Locans. "Resonance Oscillations in Sunspots." In: *Soviet Astronomy Letters* 7 (1981), pp. 25–27.

[11] J. H. Thomas. "Umbral oscillations in sunspots". In: *Astronom. Astrophys.* 135 (1984), p. 188.

[12] J. H. Thomas and M. A. Scheuer. "Umbral oscillations in a detailed model umbra". In: *Solar Phys.* 79 (1982), pp. 19–29.

[13] M. A. Scheuer and J. H. Thomas. "Umbral oscillations as resonant modes of magneto-atmospheric waves". In: *Solar Phys.* 71 (1981), pp. 21–38.

[14] D. B. Jess. et al. "A chromospheric resonance cavity in a sunspot mapped with seismology." In: *Nature Astronomy* 4 (2020), pp. 220–227.

[15] T. Felipe. "Signatures of sunspot oscillations and the case for chromospheric resonances." In: *Nature Astronomy* (2020).

[16] B. Fleck and F. L. Deubner. "Dynamics of the solar atmosphere. II. Standing waves in solar chromosphere." In: *Astron. and Astrophys.* 224 (1989), pp. 245–252.

[17] E. Khomenko and M. Collados. "Numerical modeling of Magnetohydrodynamic wave propagation and refraction in sunspots." In: *The Astrophysical Journal* 653.1 (2006).

[18] T. Felipe et al. "Magneto-acoustic waves in sunspots: First results from a new three-dimensional nonlinear Magnetohydrodynamic code". In: *The Astrophysical Journal* 719.1 (2010), pp. 357–377.

[19] P. Maltby et al. "A new sunspot umbral model and its variation with the solar cycle." In: *The Astrophysical Journal* 306 (1986), pp. 284–303.

[20] T. Felipe and C. R. Sangeetha. "Numerical determination of the cutoff frequency in solar models". In: *Astron. and Astrophys.* 640 (2020).

A Adiabatic limit for radiative losses theory

The adiabatic limit comes from considering $\tau_r = \infty$, taking limits one obtains:

$$\lim_{\tau_r \to \infty} h_R = \frac{\omega^2}{gH\gamma} - \frac{1}{4H^2} = \frac{\omega^2}{c_s^2} - \frac{1}{4H^2}$$

$$\lim_{\tau_r \to \infty} h_I = 0$$

So the components of k_z will be:

$$\lim_{\tau_r \to \infty} k_R = \Big[\frac{1}{2}\big(2 \cdot (\frac{\omega^2}{c_s^2} - \frac{1}{4H^2})\big)\Big]^{1/2} = \Big[\frac{\omega^2}{c_s^2} - \frac{1}{4H^2}\Big]^{1/2} = \Big[\frac{\omega^2}{c_s^2} - \frac{\gamma^2 g^2}{4c_s^2}\Big]^{1/2} =$$

$$= \frac{\sqrt{4\omega^2 c_s^2 - \gamma^2 g^2}}{2c_s^2} = \frac{(\omega^2 - \frac{\gamma^2 g^2}{4c_s^2})^{1/2}}{c_s} = \frac{(\omega^2 - \omega_{ac}^2)^{1/2}}{c_s}$$

$$\lim_{\tau_r \to \infty} k_I = 0$$